Investigation of the local apparent viscosity in a stirred tank with a shear-thinning fluid through particle image velocimetry

Ernest Simon, Frédéric Augier, Jérôme Morchain, Jean-Lou Pierson, Alain Liné

Chemical Engineering Research and Design 206 (2024) 378–385

Contents lists available at ScienceDirect

Chemical Engineering Research and Design

journal homepage: www.elsevier.com/locate/cherd

Investigation of the local apparent viscosity in a stirred tank with a shear-thinning fluid through particle image velocimetry

Ernest Simon [a,b,*], Frédéric Augier [b], Jérôme Morchain [a], Jean-Lou Pierson [b], Alain Liné [a]

[a] Toulouse Biotechnology Institute, Université de Toulouse, CNRS, INRAE, INSA, Toulouse, France
[b] IFP Energies nouvelles, Rond-point de l'échangeur de Solaize, BP3, Solaize 69360, France

ARTICLE INFO

Keywords:
Mixing
Shear-thinning fluid
Particle image velocimetry
Apparent viscosity
Shear rate
Stirred tank

ABSTRACT

The local apparent viscosity in a cylindrical stirred tank was investigated using Particle Image Velocimetry in a shear-thinning fluid. Two impellers were studied, a Rushton turbine for validation and an axial impeller HTPG4, for three Reynolds numbers corresponding to the transition regime between laminar and turbulent flows. Mean and instantaneous velocity contours and profiles are analysed. Then, the different contributions to the mean total kinetic energy are investigated with the HTPG4 impeller. The sensitivity of the mean apparent viscosity to the method of determining the shear rate is discussed. This work shows that the mean apparent viscosity is highly sensitive to the method of determining the shear rate. Future work will focus on improving the measurement of the local shear rate.

1. Introduction

Over the years, numerous studies have been carried out to understand and quantify the physical phenomena occurring in stirred tank. Both experimental (Yianneskis et al. (1987), Sheng et al. (2000), Sharp & Adrian (2001), Escudié et al., 2002, Baldi & Yianneskis (2003), Huchet et al. (2009), de Lamotte et al. (2018)) and numerical methods (Sbrizzai et al. (2006), Gillissen et al., 2012, Hartmann et al. (2004), Menter et al., 2005, Delafosse et al. (2008), Aubin, Xuereb, 2006, Singh et al. (2011)) were used to study stirred tank hydrodynamics with Newtonian fluids. These articles represent a small portion of the work that has been carried out. Little work has been done to understand the mixing processes of non-Newtonian fluids (Dyster et al. (1993), Arratia et al. (2006), Venneker et al. (2010), Venneker et al. (2010), Liné et al. (2013), Gabelle et al. (2013), del Pozo et al. (2020), Zhang et al. (2021), Noble et al. (2023)). In the following, we are interested in the mixing of a fluid whose viscosity varies with the shear rate. This dependence on the local shear rate leads to the coexistence of different flow regimes in the sense of the Reynolds number. The main concern is then the evaluation of the shear rate in order to estimate locally the rheological characteristics of the fluid. In Gabelle et al. (2013) and del Pozo et al. (2020), the focus is on the local study of turbulence and the determination of the local and average shear rates. Each of these works stresses that the estimation of an average shear rate is difficult due to the heterogeneity of the local shear rate, but that it is indispensable for defining the flow regime and the local apparent viscosity. The most common approach is to use Metzner-Otto's relationship which connects the average shear rate in the tank to the impeller frequency N, also known as impeller velocity.

$$\dot{\gamma}_{avg} = k_S N \tag{1}$$

The constant of proportionality k_S depends on the type of impeller ($k_S = 11.5$ for a Rushton turbine). This is only valid for Newtonian fluid in the laminar regime, but it is widely used in turbulent regime. Kelly et al., 2003 found that the Metzner-Otto correlation underestimated the average shear rate with a non-Newtonian fluid. Based on this work, Pérez et al. (2006) extended this relation to non-Newtonian fluids for turbulent regime and defined another correlation.

$$\dot{\gamma}_{SP} = 3.31 N^{1.4} \tag{2}$$

However, in both cases, the evaluation of the shear rate is based on macroscopic variables, while for a non-Newtonian fluid, the apparent viscosity μ_a depends on the local shear rate, which is heterogeneous and time dependent.

For a stirred tank, the Reynolds number is defined as follows.

$$\mathrm{Re} = \frac{\rho N D^2}{\mu} \tag{3}$$

* Corresponding author at: Toulouse Biotechnology Institute, Université de Toulouse, CNRS, INRAE, INSA, Toulouse, France.
E-mail address: ernest.simon@ifpen.fr (E. Simon).

https://doi.org/10.1016/j.cherd.2024.05.008
Received 29 November 2023; Received in revised form 14 April 2024; Accepted 6 May 2024
Available online 14 May 2024

with N the impeller speed, D the impeller diameter, ρ the density of the liquid and μ its dynamic viscosity. With Newtonian fluids, the flow is considered fully turbulent if $Re > 10^4$ and laminar if $Re < 10 - 100$. In between, the flow regime varies in the tank. It is spatially heterogeneous with turbulent flow structures in the impeller region and becomes laminar with distance with the impeller. This spatial and temporal variation in the flow regime corresponds to a transitional regime and is often observed when non-Newtonian fluids are mixed.

Experimentally, different visualization techniques are widely used in the study of stirred tank, such as Particle Image Velocimetry (PIV), hot-wire anemometry, laser Doppler velocimetry (LDV) and more recently 4D-Particle Tracking Velocimetry (Schäfer et al. (1997), Mavros (2001), Adrian (2005), Hofmann et al. (2022)). They allow the investigation of flow patterns and the acquisition of instantaneous velocity fields. These raw data are used to estimate large to small structures in the flow by processing velocities and velocity gradients.

The intention of this article is to study the sensitivity of the apparent viscosity of a shear thinning fluid to the shear rate evaluation method for flows in transitional regimes. The determination of the local velocity gradients enables the calculation of the turbulent kinetic energy and the shear rate precisely in order to assess the apparent viscosity distribution. Experimental technique such as two-dimensional, two-components (2D-2 C) PIV is used. Two impellers are studied, a conventional Rushton turbine and an axial-pump impeller traditionally used in homogeneous holding, mixing and re-suspension of solids.

2. Material and methods

2.1. Mixing tank

2D-2 C PIV measurements were conducted in a standard 30 L stirred tank open on top equipped with four equally spaced baffles (width $B = T/10$). The cylindrical vessel was made of glass and had a diameter $T =$ 0.3 m equal to the liquid height (T=H). It was placed in a cubic tank filled with water in order to minimize optical refraction caused by the curved surface of the cylindrical tank. The cubic and cylindrical vessels shared the same flat bottom. The clearance, C, was equal to the impeller diameter. In this work, a Rushton turbine, and a three-bladed axial impeller (HTPG4) with a diameter of $D = 0.1$ m ($D = T/3$) mounted at the centre were used. For each impeller, three impeller speed were chosen, respectively 250, 500 and 700 rpm and 500, 900 and 1200 rpm. Their power numbers are respectively equal to 5 and 0.67 for a turbulent regime. This velocity range enables measurements to be taken at Reynolds numbers ranging from a few hundred to over a thousand, thus covering a wide range of Reynolds in the transitional regime. Fig. 1

2.2. Working fluid

Biological media that exhibit shear-thinning behaviour (e.g. filamentous fungi, product of enzymatic hydrolysis of biomass, colloidal gels) are opaque. It is therefore necessary to use transparent model fluid to analyze the flow with flow visualization techniques such as PIV.

Carboxymethyl cellulose (CMC, Sigma Aldrich) is mixed with high purity water to create a suitable transparent model fluid that mimics the rheological behaviour of biological media found in the aforementioned industrial applications. CMC comes as a fine polymer powder. Once it is added to water, the solution was mixed 12 h and left to rest 24 h to completely hydrate the molecules. Rheological measurements were carried out using a rotational Thermo Haake rheometer with a smooth stainless-steel cone and plate (6°) at 20°C.

Fig. 1. HTPG4 impeller and Rushton turbine used in this study coated with black paint to minimize laser refraction.

Two CMC solutions were used during the experiments, one with a concentration of 1 wt %, the other with a concentration of 1.5 wt %; their rheological data are presented Fig. 2.

Shear-thinning behavior is modelled using the Carreau-Yasuda model such as

$$\mu = \mu_\infty + (\mu_0 - \mu_\infty)(1 + (\lambda\dot{\gamma})^a)^{(n-1)/a} \quad (4)$$

with $\dot{\gamma}$ (s^{-1}) the shear rate, μ_0 and μ_∞ (Pa.s) respectively the viscosities at zero and infinite shear rate, λ (s) the characteristic time, a a constant and n the power index. Note that for the two solutions the viscosity at infinite shear rate is set to $\mu_\infty = 0$.

The dynamic viscosity μ is plotted Fig. 2 (left); CMC solutions exhibit shear-thinning behavior, i.e. viscosity μ decreases above a certain critical shear rate $\dot{\gamma}$ (respectively $\dot{\gamma} > 0.1s^{-1}$ and $\dot{\gamma} > 0.4s^{-1}$ for 1.5 wt % CMC and 1 wt % CMC solutions). When $\dot{\gamma}$ is sufficiently high, Eq. 4 becomes a power-law of the following form

$$\mu = K\dot{\gamma}^{n-1} \quad (5)$$

with K a constant and n the power index. Below the critical value, solutions approach a Newtonian plateau where viscosity does not depend on $\dot{\gamma}$ ($\mu = 0.85Pa.s$ and $\mu = 2.5Pa.s$ respectively for 1 wt % and 1.5 wt % CMC solutions). One can note that the yield stress is negligible. Storage G' and loss G'' moduli are given Fig. 2 (right). They were acquired in small amplitude oscillatory shear measurements (SAOS) for different angular frequencies f. Amplitude sweep test ensured that the amplitude of the SAOS measurements remained in the linear viscoelastic domain where both moduli are constant. From SAOS, one can observe that both CMC solutions are only weakly viscoelastic.

2.3. P.I.V. system

The 2D-2 C PIV technique allows the acquisition of instantaneous velocity fields throughout a region illuminated by a planar laser sheet. To estimate locally the kinematics of the flow, the flow is seeded with particles that are neutrally buoyant and able to efficiently scatter light. Two images are then taken within a short time interval using a photographic technique to measure the positions of the particles. Each image of the pair is divided into a small interrogation area (IA) of 32×32 pixels; cross-correlation is then applied to each IA to calculate the most likely particle displacement. Table 1

In this study, the PIV system consisted of a laser and image acquisition system supplied by Dantec (Dantec Dynamics A/S). The system included a Nd:YAG laser (λ=532 nm), a synchronisation system and a charge-coupled device camera (FlowSenseEO 4 M, 2048×2048 pixels^2, raw 7.4 μm /px). Raw image processing was performed using commercial PIV software (DynamicStudio 2022a, Dantec Dynamics A/S). The frame rate was adjusted individually for each impeller speed so that the mean displacement of the particle distribution in all IA was approximately one quarter of the IA size. Post-processing via DynamicStudio used adaptive correlation analysis with 50 % overlap, where the initial IA and final IA were areas of 128×128 pixels^2 and 32×32 pixels^2, respectively. For all experiments, 6000–7000 image pairs were acquired to ensure statistical convergence of velocity, both on the mean and the gradients. The experiments are not time-resolved.

Polystyrene coated with rhodamine B beads with an average diameter of 10–20 μm (Dantec Dynamics S/A, $\lambda_{emission}$=590 nm) were used as seeding particles. They have a short relaxation time to follow the motion of the flow.

2D-2 C PIV provided the instantaneous radial and axial velocity

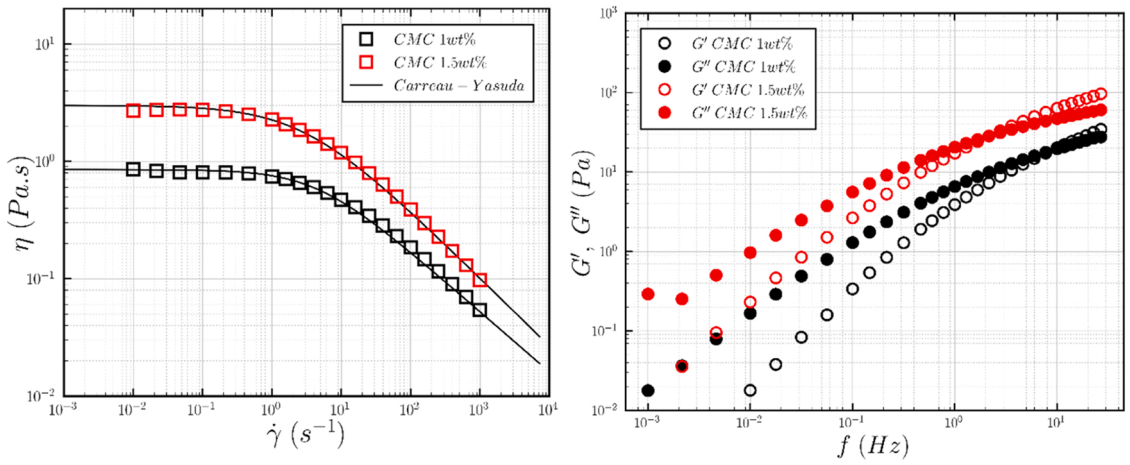

Fig. 2. Rheological profiles of CMC solutions with a calibrated Carreau-Yasuda (CY) model.

Table 1
Data-fitted parameters for the Carreau-Yasuda and power-law models.

Solution	n (-)	K ($Pa.s^n$)	a (-)	λ (s)
CMC 1 wt %	0.48	1.8	0.75	0.34
CMC 1.5 wt %	0.42	5.5	0.94	0.22

components u and *w* in a vertical plane centred on the impeller axis. The reference frame is a (X,Z) cartesian frame whose origin is located on the shaft axis at the disc level for the Rushton turbine and on the shaft axis at the end of the shaft for the HTPG4 impeller. The measurement plane was located close to the impeller, in the region of the radial jet for the Rushton turbine in front of a baffle and below the impeller in one half of the tank mid-way between two baffles for the HTPG4 impeller. The measurement planes were 4×4 cm^2 and 8×8 cm^2 respectively. Fig. 3 shows the location of the measurement planes for both impellers.

To evaluate the accuracy of the experiments, the size of the interrogation area is compared to the characteristic flow scales, i.e., the Taylor micro-scale λ_T and Kolmogorov scale η. These characteristic turbulent lengths are estimated *a posteriori* using the turbulent kinetic energy k and local dissipation rate of kinetic energy ε such as $\eta = \overline{\left((\mu/\rho)^3/_{\varepsilon}\right)^{1/4}}$ *and* $\lambda_T = \overline{\left(10\nu k/_{\varepsilon}\right)^{1/2}}$ The interrogation area Δ_{PIV} is equal to 1.9 mm and is ten times smaller than smallest Taylor micro-scale. It means that measurement of turbulent kinetic energy is, in our configuration, precise. Besides, the smallest Kolmogorov scale is about 0.8 mm corresponding to a ratio $\Delta_{PIV}/\eta \sim 2.4$. To achieve 90 % accuracy in the energy dissipation measurement, Saarenrinne et al. (2001) and Baldi, Yianneskis, 2004 stated that the spatial resolution should be around 2η. Therefore, the smallest turbulent scales are caught by the measurements.

3. Results and discussion

3.1. Mean flow

The mean flow velocity components are derived by a classical averaging of the instantaneous velocity fields. It is defined at each point (x,z) as:

$$\overline{u_i}(x,z) = \frac{1}{n}\sum_{k=1}^{n} u_{i,k}(x,z) \quad i = x,z. \tag{6}$$

k represents the kth event measured. If the measurements were time-resolved, k would represent time.

In Fig. 4 the instantaneous velocity magnitudes and vectors are plotted for CMC 1 wt % and Rushton turbine at 250, 500 and 700 rpm. The velocity magnitude u_{mag} and its mean $\overline{u}_{mag}$ are defined respectively as $u_{mag} = \sqrt{u^2 + w^2}$ and $\overline{u}_{mag} = \sqrt{\overline{u}^2 + \overline{w}^2}$. From Eqs. 1, 3 and 5, modified generalized Reynolds number can be defined as

$$Re = \frac{\rho N^{2-n} D^2}{K k_S^{n-1}}. \tag{7}$$

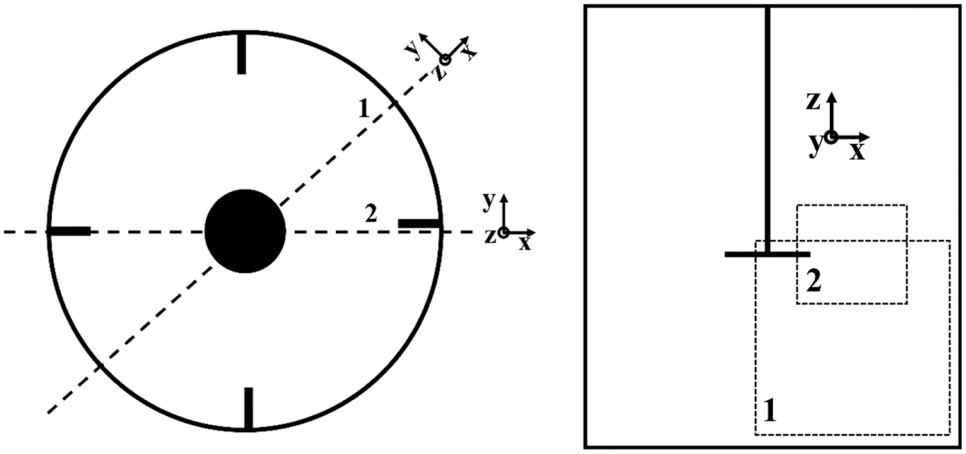

Fig. 3. Measurement planes: Rushton turbine (2), HTPG4 (1), horizontal (left) and vertical view (right).

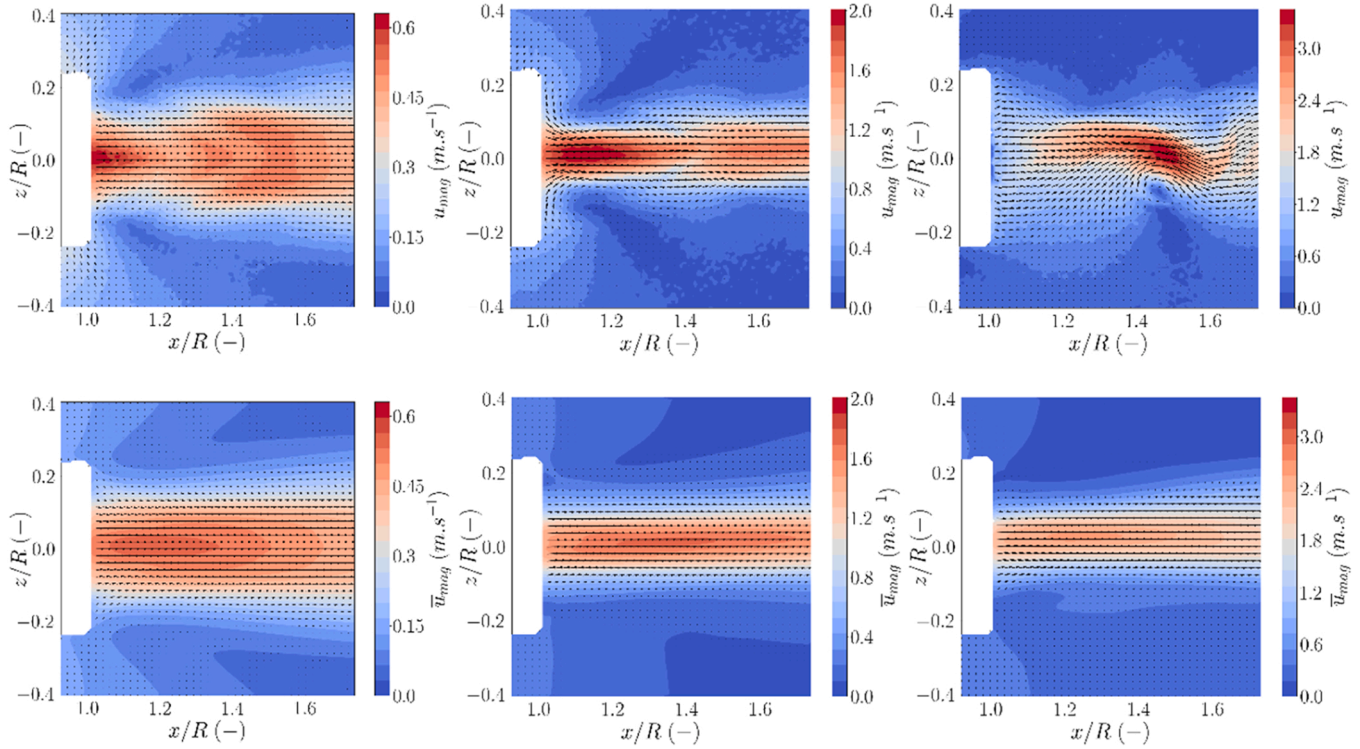

Fig. 4. Rushton turbine: Instantaneous (top) and mean (bottom) velocity contour along with vector plots in plane YZ (X=0 mm) for 250, 500 and 700 rpm. Each arrow starts from the grid point represented with its arrowhead proportional to its magnitude.

It corresponds to Reynolds numbers of 340, 980 and 1640 respectively for 250, 500 and 750 rpm. The flow near the impeller for each configuration is in agreement with the classical results in the literature (Gabelle et al. (2013), del Pozo et al. (2020)). The radial velocity component is predominant, as indicated by the presence of a radial jet. It can be observed that at a low impeller speed of 250 rpm, the radial jet tends to be thicker than at 500 and 700 rpm, and no vortex structures seem to detach from the agitation zone. As the impeller angular velocity is increased, instabilities in the velocity flow appear and the velocity magnitude reaches higher values in the core of the radial jet.

In Fig. 5, vertical profiles of the ensemble averaged radial u/u_{tip} and axial w/u_{tip} velocity components are plotted against the normalised vertical coordinate $z^* = z/R$ for a radial position close to the impeller x/R=1.07. u_{tip} is the impeller tip speed and is defined as $u_{tip} = \pi DN$.

The maximum normalized velocity in water is close to 0.7, in agreement with with Escudié & Liné (2003) and Gabelle et al. (2013), where the normalised maximum mean radial velocities are 0.74 and 0.76, respectively, at the same radial position $x/R = 1.07$ at Re $\sim$ 56000. The slight differences in maximum velocity are due to the geometry of the tanks, which are not exactly the same in previous works. For CMC 1 wt %, the radial velocity profiles at 500 and 700 rpm are quite similar, while a decrease in the maximum radial velocity is observed at 250 rpm. This tends to indicate that the flow regime at the lowest velocity is different from that at 500 and 700 rpm. It can be seen that the angle of the radial jet increases as the impeller speed increases. The vertical profiles therefore clearly show the influence of rheology on the mean flow. For CMC 1 wt % and at impeller level, the axial velocity is zero at 250 rpm, indicating that the flow in this configuration is purely radial. In addition, it can be noted that in Fig. 5, axial profiles of mean

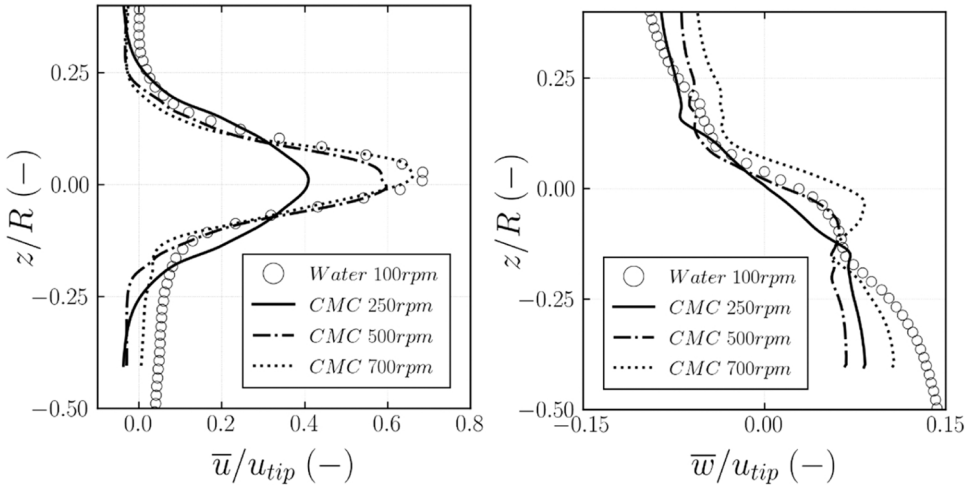

Fig. 5. Normalized vertical profiles of mean radial u and axial w velocity components for a radial position x/R=1.07.

radial velocity profiles in water at 100 rpm and in CMC at 700 rpm almost overlap. Near the impeller blades and at high impeller speed, viscous effects are no longer predominant, and the flow is locally close to that encountered with a Newtonian fluid.

The instantaneous velocity magnitudes and vectors are plotted in Fig. 6 for CMC 1 wt % and HTPG4 impeller at 500, 900 and 1200 rpm. With the HTPG4 impeller, it is more difficult to evaluate the generalized Reynolds number since k_S is unknown. However, based on Eq. 7, the generalized Reynolds number is multiplied by a factor 4 between 500 and 1200 rpm. A thin downward axial-radial flow is observed at 500 rpm, but it rapidly weakens with distance from the impeller. Viscous effects appear to dominate pressure effects at 500 rpm. However, as the impeller speed increases, the downward jet develops continuously, overcoming the viscous effects, and at 1200 rpm vortex structures interact with the flat bottom of the vessel. Preliminary PIV measurements on large field of view (not shown here) show that the mean flow is axisymmetric at each velocity. For Newtonian fluids, the HTPG4 impeller produces a pure axial flow; the influence of shear-thinning rheology is highlighted by the evolution of the downward jet in terms of length and direction. Contour maps of the mean kinetic energy (provided as Supplementary material) show that most of the kinetic energy transported by the jet is contained in the centre of the downward jet.

Horizontal profiles ($z^* = \frac{z}{R} = -0.6$) of the kinetic energy are shown on Fig. 7. Due to the 2D in-plane measurements., the kinetic energy is determined without the contribution of the circumferential velocity and therefore its reconstruction is incomplete. $\overline{K}_{tot}$ is defined as $\overline{K}_{tot} = \frac{1}{2}\overline{u^2 + w^2} = \frac{1}{2}\left(\overline{u}^2 + \overline{w}^2 + \overline{u'^2 + w'^2}\right) = \overline{K} + k$. As expected, the turbulent kinetic energy k is at least one order of magnitude lower than the mean kinetic energy $\overline{K}$ which represents most of the mean total kinetic energy $\overline{K}_{tot}$. At 500 rpm, $\overline{K}_{tot}$ and $\overline{K}$curves overlap, whereas at 900 and 1200 rpm, $\overline{K}_{tot} > \overline{K}$. It appears that for each configuration, there is a peak of mean kinetic energy; whose location varies for all impeller speed. The axial component fixes the location of the peak; at 500 rpm, radial and axial components are equivalent, as the impeller speed increases however, axial component becomes predominant while the radial component rapidly decays. These results are in agreement with Del Pozo et al. (2020).

3.2. Viscosity

The most rigorous determination of the local viscosity relies upon the local and instantaneous shear rate using local and instantaneous velocity gradients. The shear rate can be evaluated locally as

$$\dot{\gamma_i}^2 = 2S_{ij}S_{ij} \tag{8}$$

The instantaneous strain rate tensor S_{ij} is defined as

$$S_{ij} = \frac{1}{2}\left(\frac{\partial u_i}{\partial x_j} + \frac{\partial u_j}{\partial x_i}\right) \tag{9}$$

In-plane P.I.V. measurements provide incomplete information on velocity, only two components of velocity are measured. Therefore, only four of the nine components of the deformation tensor can be calculated directly, and a fifth one can be evaluated by assuming zero velocity divergence. In 2D-2 C P.I.V., the instantaneous local total shear can be reconstructed as

$$\dot{\gamma_i}^2 = 2\left(\frac{\partial u}{\partial x}\right)^2 + 2\left(\frac{\partial w}{\partial z}\right)^2 + 2\left(\frac{\partial v}{\partial y}\right)^2 + \left(\frac{\partial w}{\partial x} + \frac{\partial u}{\partial z}\right)^2 \tag{10}$$

This information can be used to compute the local viscosity field at each instant form and its time averaged value as

$$\overline{\mu} = \overline{\mu_\infty + (\mu_0 - \mu_\infty)\left(1 + \left(\lambda\sqrt{\dot{\gamma_i}^2}\right)^a\right)^{(n-1)/a}} \tag{11}$$

The time-averaged viscosity field can also be computed from the time-average of instantaneous gradients

$$\overline{\mu} = \mu_\infty + (\mu_0 - \mu_\infty)\left(1 + \left(\lambda\sqrt{\overline{\dot{\gamma_i}^2}}\right)^a\right)^{(n-1)/a} \tag{12}$$

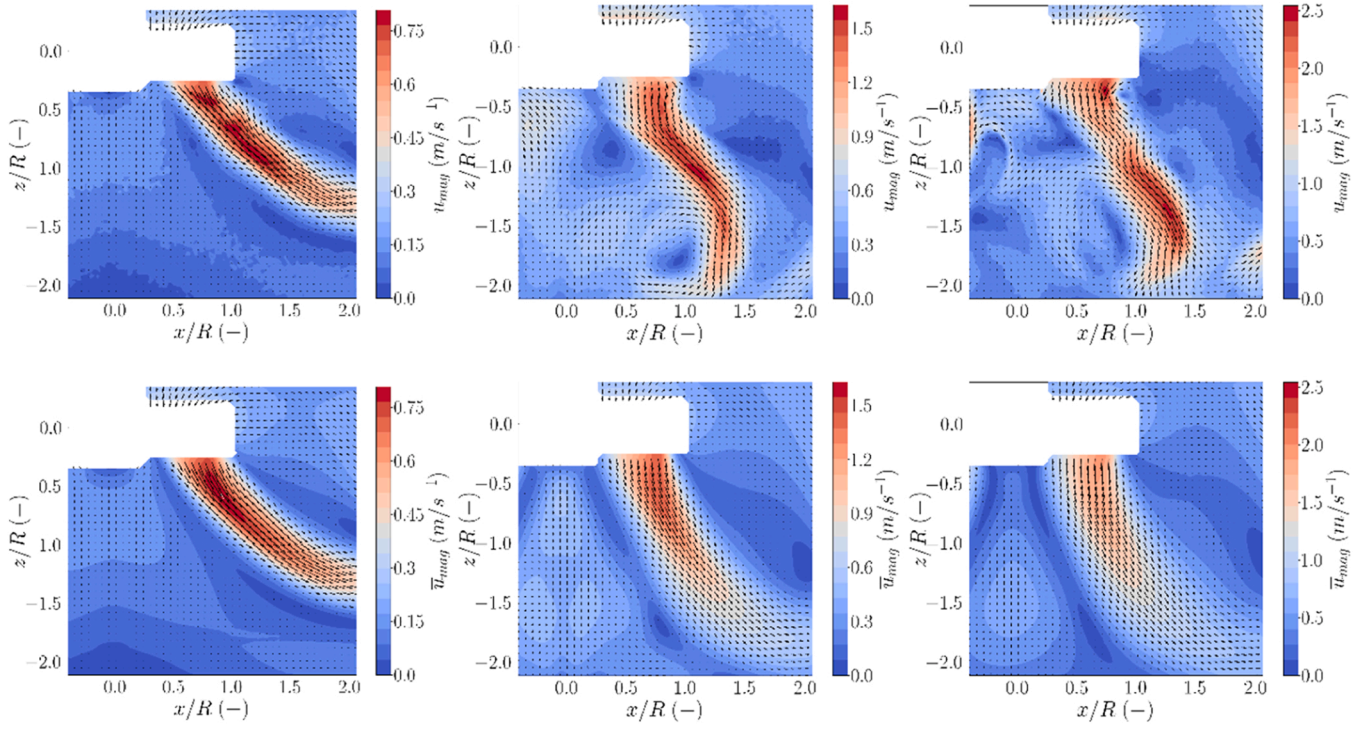

Fig. 6. HTPG4 impeller: Instantaneous (top) and mean (bottom) velocity contours and vector plots in plane YZ (X=0 mm) for 500, 900 and 1200 rpm. Each arrow starts from the grid point represented with its arrowhead proportional to its magnitude.

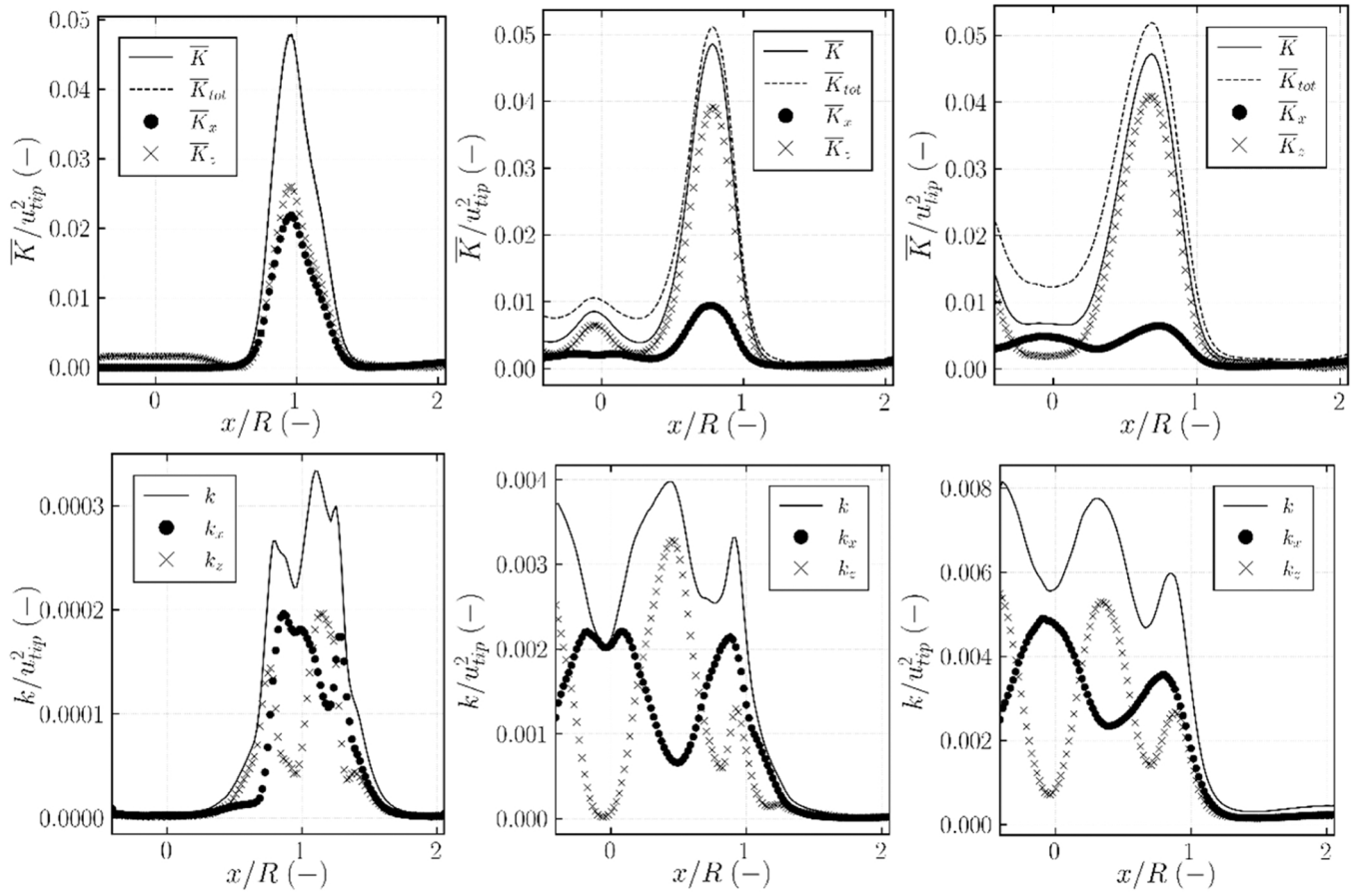

Fig. 7. Kinetic energy profiles at z*=-0.6 below the impeller for 500 (left), 900 (centre) and 1200 rpm (right).

Both previous methods rely upon the knowledge of instantaneous velocity gradients. The third method would consist in computing the shear rate from the gradients of time-averaged velocities to estimate the viscosity field.

$$\overline{\mu} = \mu_\infty + (\mu_0 - \mu_\infty)(1 + (\lambda\dot{\overline{\gamma}})^a)^{(n-1)/a} \quad (13)$$

The aim of the following discussion is to evaluate the spatial distribution of the mean apparent viscosity (derived directly from Eq. 4). It depends directly on the shear rate $\dot{\gamma}$, i.e. velocity gradients. Instantaneous velocity gradients are available and it is worth comparing the evaluation of the mean apparent viscosity with three different statistical methods using (a) the instantaneous local shear rate $\sqrt{\dot{\gamma}_i^{\,2}}$ (Eq. 11), (b) the averaged instantaneous local shear rate $\sqrt{\overline{\dot{\gamma}_i}^{\,2}}$ (Eq. 12) and (c) the shear rate obtained from averaged velocity gradients (Eq. 13). It must be noted that the first method is the most rigorous since the average apparent viscosity is directly based on its local values. The last method of evaluating the apparent mean viscosity based on mean velocity gradients is sometimes used in numerical simulations with the RANS (or URANS) method. With RANS methods, the dissipation ε is expressed as $\varepsilon = 2\nu_a\overline{s'_{ij}}^{\,2}$ and the production of kinetic energy is defined as $2\nu_t\overline{S_{ij}}^{\,2}$. If the dissipation equals the production of kinetic energy, the equality can be rewritten as $\dot{\gamma}_i^{\,2} = \frac{\nu_t}{\nu_a}\overline{S_{ij}}^{\,2}$ where $\overline{S_{ij}}$ depends directly on mean velocity gradients $\frac{\partial\overline{u}_i}{\partial x_j}$. It appears that, when the flow is not in laminar regime, there is a factor $\sqrt{\frac{\nu_t}{\nu_a}}$ between the local and instantaneous shear rate and the mean shear rate. This analysis shows that shear rate determination based on mean velocity gradients can have a significant impact on the value of local apparent viscosity. This is what is shown below.

Local distribution of mean apparent viscosity obtained with the three different approaches for an impeller speed of 1200 rpm is plotted Fig. 8. Viscosity distribution is "highly" heterogenous. Directly under the impeller, mean viscosity reaches its lowest value ($\overline{\mu}\left(\sqrt{\dot{\gamma}_i^{\,2}}\right) \sim 0.14$ Pa. s). Close to the impeller, velocity fluctuations are high, creating intense velocity gradients. At the impeller tip, the viscosity increases rapidly with the distance from the impeller. At 1200 rpm, the contribution of radial velocity to the turbulent kinetic energy is negligible compared to the axial velocity contribution; gradients in the radial direction are less intense and the apparent viscosity reaches high values quickly. This is consistent with previous observations that vortex structures develop below the impeller, the flow is predominantly axial and the radial component of the velocity has a small magnitude. The low viscosity region corresponds to the downward jet. Comparing the mean viscosity distributions obtained by methods (a) and (b), it appears that the spatial distributions are qualitatively similar, but not quantitatively. In fact, the mean viscosity is underestimated when the averaged instantaneous local shear rate is used. Near the impeller and at the downward jet edges the correct mean viscosity is 20 %-25 % higher, while in the centre of the downward jet the discrepancy is about 15 %. The viscosity distribution from the third method does not agree qualitatively or quantitatively with the correct method with a minimum overestimation on the viscosity of 30 %. Local viscosities are greatly overestimated. The shear rate obtained from mean velocity gradients is therefore insufficient to accurately assess the local viscosity distribution. The overestimation of local viscosity in the impeller jet decreases with the Reynolds number, from 30 % to 15 % at 500 rpm. This result shows that the contribution of the velocity gradient fluctuations to the shear rate is more significant than the contribution of the mean velocity field. It is coherent with the previous analysis on the ratio existing between the local and

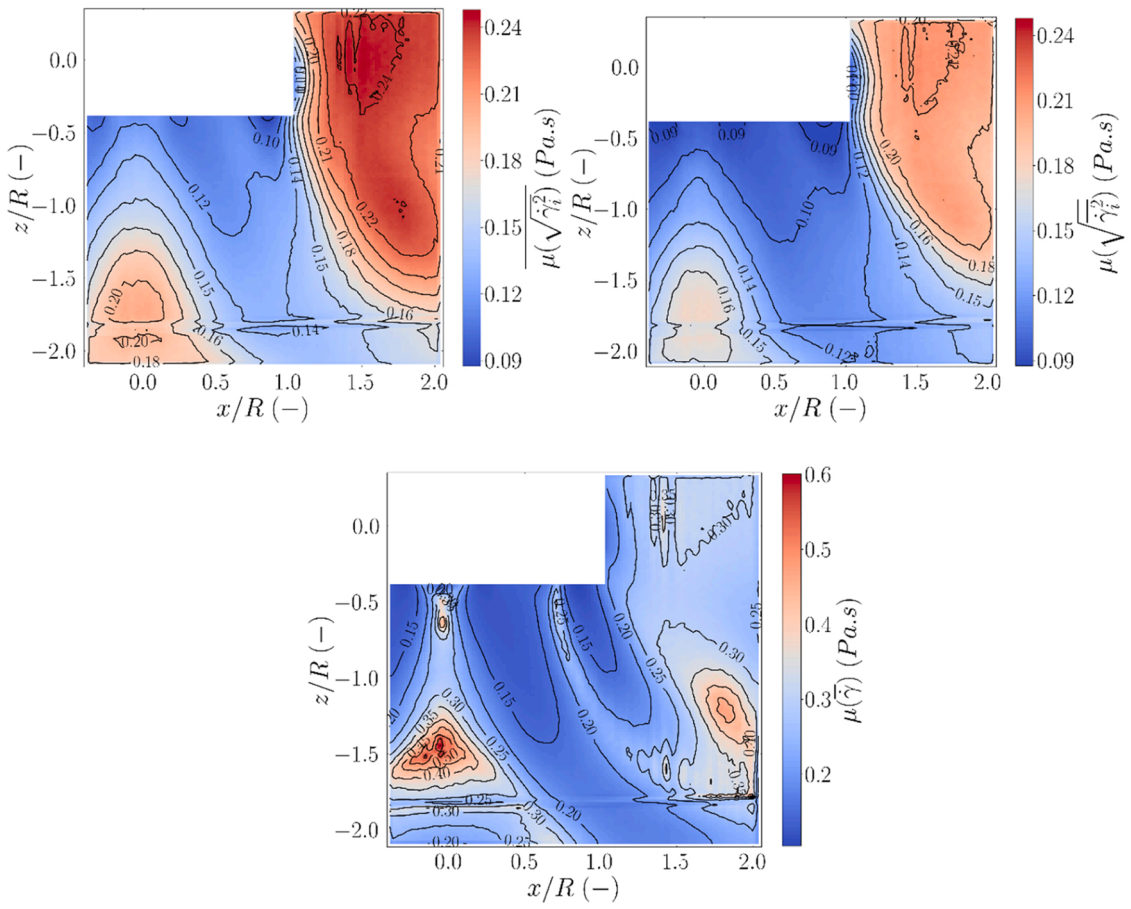

Fig. 8. Contours of mean apparent viscosity calculated with method (a), (b) and (c).

instantaneous shear rate and the mean shear rate. When the flow is turbulent, the ratio between ν_a and ν_t is large according to the so-called local equilibrium hypothesis and tends to decrease with the Reynolds number. This is observed when the Reynolds number is increased by a factor 4 between 500 rpm and 1200 rpm.

The predicted average viscosity based on Eq. 1 and Eq. 4 is equal to 0.16 Pa.s. The viscosity prediction based on the Metzner-Otto correlation largely overestimates the values of apparent viscosity obtained from experimental data in the region where the shear rate is non-negligible, i.e., in the impeller jet. As highlighted in Gabelle *et al.* (2012) and Del Pozo et al. (2020), the estimation of an averaged shear rate is the stirred tank is difficult due to the heterogeneity of the shear rate in the whole tank.

4. Conclusions

In this study, the mixing of a shear-thinning fluid (aqueous CMC solution) in a stirred tank has been investigated in the transition regime with a Rushton turbine and an HTPG4 impeller. The rheological parameters of the non-Newtonian fluid were measured to relate the shear rate and the apparent viscosity.

2D-2 C P.I.V. measurements were performed below the impeller and in the discharge region respectively with the HTPG4 impeller and the Rushton turbine at three impeller speed for each impeller.

The mean flow was evaluated in terms of velocity profiles and spatial distributions from instantaneous velocity fields. They were compared to water measurements and to published work. The influence of the rheology was underlined. With the Rushton turbine, the increase of the impeller velocity is accompanied by an intensification of vortical structure detachment, and the core of the discharge jet is confined to a region centred on the impeller blade. With the HTPG4 impeller, the axial velocity component becomes dominant as the impeller speed increases highlighting that viscous effects become negligible compared to pressure effects.

The spatial distribution of the apparent viscosity was carefully studied. Its evaluation was done based on three different statistical methods on the determination of the shear rate. It was underlined that the evaluation based on the mean velocity gradients overestimates the average apparent viscosity and fails to predict its spatial distribution. The method based on the mean instantaneous shear rate manage to predict qualitatively the apparent viscosity spatial distribution but underestimates the local values. This work highlights the sensitivity of estimating the average apparent viscosity in stirred tank. Even if the shear rate is measured with accuracy, the treatment of the measurement influences the determination of apparent viscosity.

2D-2 C P.I.V. enables the measurement of only two components of the velocity. The next part of the experimental work focuses on improving the accuracy of the measurement of the local shear rate. 2D-3 C P.I.V. measurements will be carried out to have access to the tangential velocity component in the radial and axial directions. The final step of this study is to use TOMO-PTV (Tomographic Particle Tracking Velocimetry). to retrieve a complete information on velocity components in the three spatial directions. The last four components of the strain rate tensor will be known allowing a precise measurement of the shear rate. The same analysis on mean velocity and apparent viscosity determination will be carried out to evaluate the influence of the tangential velocity component on both quantities.

This work also furnishes quantitative data that can be used to validate CFD investigations on the agitation of non-Newtonian fluids in stirred tank.

CRediT authorship contribution statement

Jérôme Morchain: Investigation, Methodology, Supervision, Validation, Writing – review & editing. **Ernest Simon:** Conceptualization, Data curation, Formal analysis, Methodology, Validation, Writing – original draft, Writing – review & editing. **Jean-Lou Pierson:** Funding acquisition, Project administration, Resources, Supervision, Writing – review & editing. **Frédéric Augier:** Conceptualization, Funding acquisition, Investigation, Methodology, Validation, Writing – review & editing. **Alain Liné:** Conceptualization, Methodology, Validation, Writing – review & editing, Data curation, Investigation, Supervision.

Declaration of interest

The authors declare that they have no known competing financial interests or personal relationships that could have appeared to influence the work reported in this paper.

Acknowledgement

This work was supported by IFP Energies Nouvelles (IFPEN).

References

Adrian, R., 2005. Twenty years of particle image velocimetry. Exp. Fluids. https://doi.org/10.1007/s00348-005-0991-7.

Arratia, P.E., Kukura, J., Kukura, J., Lacombe, J.P., Muzzio, F.J., 2006. Mixing of shear-thinning fluids with yield stress in stirred tanks. AIChE J. https://doi.org/10.1002/aic.10847.

Aubin, J., Xuereb, C., 2006. Design of multiple impeller stirred tanks for the mixing of highly viscous fluids using CFD. Chem. Eng. Sci. https://doi.org/10.1016/j.ces.2005.10.075.

Baldi, S., Yianneskis, M., 2003. On the direct measurement of turbulence energy dissipation in stirred vessels with PIV. Ind. Eng. Chem. Res. https://doi.org/10.1021/ie0208265.

Baldi, S., Yianneskis, M., 2004. On the quantification of energy dissipation in the impeller stream of a stirred vessel from fluctuating velocity gradient measurements. Chem. Eng. Sci. https://doi.org/10.1016/j.ces.2004.03.021.

de Lamotte, A., Delafosse, A., Calvo, S., Toye, D., 2018. Analysis of PIV measurements using modal decomposition techniques, POD and DMD, to study flow structures and their dynamics within a stirred-tank reactor. Chem. Eng. Sci. https://doi.org/10.1016/j.ces.2017.12.047.

del Pozo, D.F., Liné, A., Geem, K.V., Men, C.L., Nopens, I., Nopens, I., 2020. Hydrodynamic analysis of an axial impeller in a non-newtonian fluid through particle image velocimetry. AIChE J. https://doi.org/10.1002/aic.16939.

Delafosse, A., Delafosse, A., Liné, A., Liné, A., Morchain, J., Morchain, J., Guiraud, P., 2008. LES and URANS simulations of hydrodynamics in mixing tank: comparison to PIV experiments. Chem. Eng. Res. Des. https://doi.org/10.1016/j.cherd.2008.07.008.

Dyster, K.N., Koutsakos, E., Jaworski, Z., Nienow, A.W., 1993. An LDA study of the radial discharge velocities generated by a Rushton turbine: newtonian fluids, Re $\geq$ 5. Chem. Eng. Res. Des.

Escudié, R., Escudié, R., Escudié, R., Liné, A., Liné, A., 2002. Experimental analysis of hydrodynamics in a radially agitated tank. AIChE J. https://doi.org/10.1002/aic.690490306.

Gabelle, J.-C., Morchain, J., Morchain, J., Anne-Archard, D., Augier, F., Liné, A., Liné, A., 2013. Experimental determination of the shear rate in a stirred tank with a non-newtonian fluid: carbopol. AIChE J. https://doi.org/10.1002/aic.13973.

Gillissen, J.J., Gillissen, J.J., van den Akker, H.E., 2012. Direct numerical simulation of the turbulent flow in a baffled tank driven by a Rushton turbine. AIChE J. https://doi.org/10.1002/aic.13762.

Hartmann, H., Derksen, J., van den Akker, H.E., 2004. Macroinstability uncovered in a Rushton turbine stirred tank by means of LES. AIChE J. https://doi.org/10.1002/aic.10211.

Hofmann, S., Weiland, C., Fitschen, J., von Kameke, A., Hoffmann, M., Schlüter, M., 2022. Lagrangian sensors in a stirred tank reactor: comparing trajectories from 4D-particle tracking velocimetry and lattice-boltzmann simulations. Chem. Eng. J. *449*, 137549 https://doi.org/10.1016/j.cej.2022.137549.

Huchet, F., Huchet, F., Liné, A., Morchain, J., 2009. Evaluation of local kinetic energy dissipation rate in the impeller stream of a Rushton turbine by time-resolved PIV. Chem. Eng. Res. Des. https://doi.org/10.1016/j.cherd.2008.11.012.

Kelly, W., Kelly, W.J., Gigas, B., 2003. Using CFD to predict the behavior of power law fluids near axial-flow impellers operating in the transitional flow regime. Chem. Eng. Sci. https://doi.org/10.1016/s0009-2509(03)00060-5.

Liné, A., Gabelle, J.-C., Morchain, J., Anne-Archard, D., Augier, F., 2013. On POD analysis of PIV measurements applied to mixing in a stirred vessel with a shear thinning fluid. Chem. Eng. Res. Des. https://doi.org/10.1016/j.cherd.2013.05.002.

Mavros, P., 2001. Flow visualization in stirred vessels a review of experimental Techniques. Chem. Eng. Res. Des. https://doi.org/10.1205/02638760151095926.

Menter, F.R., Menter, F.R., Egorov, Y., 2005. A scale-adaptive simulation model using two-equation models. null. https://doi.org/10.2514/6.2005-1095.

Noble, S., Poirier, M., Thomas, J., 2023. Blending and cavern formation within non-Newtonian fluids in stirred tanks: application to nuclear waste fluid processing. Chem. Eng. Sci. *266*, 118184.

Pérez, J.A., Porcel, E.M., López, J.L., Sevilla, J.M., Chisti, Y., 2006. Shear rate in stirred tank and bubble column bioreactors. Chem. Eng. J. https://doi.org/10.1016/j.cej.2006.07.002.

Saarenrinne, P., Piirto, M., Eloranta, H., 2001. Experiences of turbulence measurement with PIV. Meas. Sci. Technol. *12*, 1904.

Sbrizzai, F., Lavezzo, V., Verzicco, R., Campolo, M., Soldati, A., 2006. Direct numerical simulation of turbulent particle dispersion in an unbaffled stirred-tank reactor. Chem. Eng. Sci. https://doi.org/10.1016/j.ces.2005.10.073.

Schäfer, M., Höfken, M., Durst, F., 1997. Detailed LDV measurements for visualization of the flow field within a stirred-tank reactor equipped with a Rushton turbine. Chem. Eng. Res. Des. https://doi.org/10.1205/026387697524399.

Sharp, K.V., Adrian, R., 2001. PIV study of small-scale flow structure around a Rushton turbine. AIChE J. https://doi.org/10.1002/aic.690470403.

Sheng, J., Meng, H., Fox, R.O., 2000. A large eddy PIV method for turbulence dissipation rate estimation. Chem. Eng. Sci. https://doi.org/10.1016/s0009-2509(00)00039-7.

Singh, H., Singh, H., Fletcher, D.F., Nijdam, J.J., 2011. An assessment of different turbulence models for predicting flow in a baffled tank stirred with a Rushton turbine. Chem. Eng. Sci. https://doi.org/10.1016/j.ces.2011.08.018.

Venneker, B.C., Derksen, J., den Akker, H.E., 2010. Turbulent flow of shear-thinning liquids in stirred tanks—The effects of Reynolds number and flow index. Chem. Eng. Res. Des. https://doi.org/10.1016/j.cherd.2010.01.002.

Yianneskis, M., Popiolek, Z., Whitelaw, J.H., 1987. An experimental study of the steady and unsteady flow characteristics of stirred reactors. J. Fluid Mech. https://doi.org/10.1017/s002211208700051x.

Zhang, Y., Wang, L., Huo, H., Li, Z., Gao, Z., 2021. Computational and experimental investigation of flow fields in a Rushton turbine stirred tank with shear-thinning fluid. Asia Pac. J. Chem. Eng. https://doi.org/10.1002/apj.2735.